Biophysics

Volume 2, Issue 3, 259-273.
DOI: 10.3934/biophy.2015.3.259
Received date 26 March 2015,
Accepted date 9 July 2015,
Published date 12 July 2015

http://www.aimspress.com/

Research article

Cryo-STEM Tomography of Intact Vitrified Fibroblasts

David Kirchenbuechler [1,†], Yael Mutsafi [2,†], Ben Horowitz [2],Smadar Levin-Zaidman [3], Deborah Fass [2], Sharon G. Wolf [3], and Michael Elbaum [1,*]

[1] Department of Materials and Interfaces, Weizmann Institute of Science, Rehovot 7610001
[2] Department of Structural Biology, Weizmann Institute of Science, Rehovot 7610001
[3] Electron Microscopy Unit, Chemical Research Support Department, Weizmann Institute of Science, Rehovot 7610001

[†] **equal contribution**

* **Correspondence:** Email: michael.elbaum@weizmann.ac.il; Tel: +97-289-343-537.

Abstract: Cryo-tomography of intact, vitrified cells provides a three dimensional view of their structure and organization in a snapshot of the living state. Lacking heavy metal stains, tilt series images are typically produced by defocus phase contrast. Recently, a number of other methods have been introduced for 3D cryo-imaging. These include phase plate imaging, soft X-ray tomography, serial surface imaging using the focused ion beam-scanning electron microscope, and cryo-STEM tomography (CSTET). Here we explain the basis of the STEM setup and demonstrate the capabilities of CSTET to study unfixed, fully hydrated mammalian cells. Numerous cellular features are recognized in CSTET reconstructions, including membranes, vesicles, cytoskeleton, extracellular matrix, coated pits, and ribosomes. STEM signal acquisition configuration is more flexible than defocus phase contrast, and it imposes a much less severe spatial filter on the original images. Because low spatial frequency information is retained, the STEM tomographic reconstruction more faithfully represents the mass density distribution in the specimen.

Keywords: 3DEM; cryo-tomography; scanning transmission electron microscopy; cryo-electron tomography; CSTET; organelles; mycoplasma

1. Introduction

Electron microscopy (EM) of biological systems is in the midst of major developments on multiple fronts. Introduction of the direct electron detector technology has enabled structural characterization of large proteins at resolutions previously obtainable only by X-ray crystallography [1,2]. Obviating the need for crystallization and easing requirements for rigorous purification, the way is open to study a far wider range of macromolecules and macromolecular complexes at high resolution. Furthermore, structure determination by EM in principle gives access to a broader and more realistic range of macromolecular conformations than those amenable to trapping in crystal lattices. The second area of advance in EM encompasses methods for studying intact cellular structures and imaging macromolecular complexes embedded in their functional cellular contexts. In special cases such as thin bacteria [3] or pico-eukaryotes [4], even entire cells can be studied by transmission electron microscope (TEM) tomography without sectioning, using standard defocus phase contrast, or more recently using newly available phase plates [5–8]. Sub-tomogram averaging of structures detected within cells by cryo-tomography brings the power of single-particle reconstruction processing to a growing number of important *in situ* complexes and organelles [9].

The possibilities for three dimensional imaging of vitrified specimens, i.e., cryo-tomography in various forms, have expanded significantly in recent years. Introduction of the focused ion beam scanning electron microscope (FIB-SEM) with cryogenic sample handling enables the preparation of vitreous sections for tomography guided by correlative light microscope imaging. Thus one can focus the detailed 3D analysis on specific areas of interest [10–12]. Other advances take fundamentally different approaches to volume imaging. These include soft X-ray cryo-tomography [13–17], full cryogenic serial surface imaging within the FIB-SEM [18], and most recently cryo-tomography using the scanning transmission modality [19]. Each of these methods offers an extension of cryo-tomography to somewhat different realms. Moreover, each relies on a different physical interaction between the illuminating radiation and the specimen, so fundamentally different properties are represented in the image contrast. None of the newer methods is yet as mature as phase contrast TEM, so an appreciation of the various capabilities and the relative advantages of each will emerge over time.

This contribution reports on progress in the CSTET (Cryo-Scanning Transmission Electron Tomography) method for cellular imaging. The advantages of scanning transmission electron microscopy (STEM) for tomography of plastic-embedded sections have been amply demonstrated [20–22]. Recently we have extended the STEM approach to full cryo-tomography in the CSTET method [19]. While our previous report focused on bacterial samples, we demonstrate here that CSTET is indeed a practical modality for 3D imaging of intact, unfixed, vitrified mammalian tissue culture cells. Thicker regions of the cell are accessible using CSTET than using phase contrast due to the different mechanisms of image formation. Specifically, STEM forms a raster image on the basis of point- by- point electron scattering measurements. Without an imaging lens, the blurring effects of inelastic scattering and chromatic aberration are eliminated. The optical map relating specimen density to image pixel value in STEM is also simpler than in defocus phase contrast. STEM images are free of the oscillations of the phase contrast transfer function (CTF), which invert bright and dark depending on spatial frequency. Moreover, the low spatial frequency information is retained in STEM, whereas defocus phase contrast effectively imposes a high-pass

filter. As a result, STEM images in focus provide a more faithful representation of the mass distribution in the specimen.

In the following we explore the contrast obtained from various cellular components as observed *in situ*: membranes, cytoskeleton, ribosomes, and extracellular matrix. The emphasis here is on field of view and cellular context rather than reaching the maximum obtainable resolution. We then discuss the methodology in general terms, comparing the image formation process with the more familiar EM techniques. While a full theoretical justification is beyond the present scope, the simple considerations presented in the discussion provide sufficient insight to interpret the images and to appreciate the potential for further development.

2. Materials and Method

2.1. Cell culture and sample preparation

WI-38 embryonic lung fibroblasts were obtained from Coriell, passage 12. Frozen aliquots were thawed and cultured in full MEM medium (Gibco) with 15% fetal calf serum (Gibco) at 37 °C in 5% CO_2. A maximum of 5 passages were performed, after which a new culture was started. For cryo-tomography, gold Quantifoil R3.5/1 grids were prepared by plasma treatment (10 mA for 1 minute), followed by application of 20 nm colloidal gold in phosphate buffered saline for use as fiducial markers. Grids were resterilized by UV exposure before plating of cells, which were then grown to approximately 70% confluence. Grids were blotted and plunged into liquid ethane using a Leica EM plunger and stored in liquid nitrogen until use. For preparation of thin sections, the cells were grown on glass coverslips, fixed using 2.5% gluteraldehyde, 2% paraformaldehyde in 0.1 M sodium cacodylate buffer at room temperature, washed in cacodylate buffer at 4 °C, and stained with 1% osmium tetroxide and 2% uranyl acetate. Samples were dehydrated in cold ethanol and then embedded in Epon. After removing the glass coverslips with liquid nitrogen, ultrathin sections of the monolayer Epon blocks (~70 nm) were cut either parallel or perpendicular to the cover slip surface and transferred to 200 mesh copper grids. Thin plastic sections were imaged in a FEI Tecnai Spirit T-12 operated at a 120 kV. Images were recorded by 2k Eagle CCD camera (FEI, Eindhoven) or by a side-mounted Mega View TEM CCD (SIS).

2.2. Cryo-scanning transmission electron tomography (CSTET)

Vitrified fibroblast samples were observed with a Tecnai F20 S/TEM instrument at 200 kV. CSTET was performed with extraction voltage = 4300 V, gun lens = 6, and spot size = 5, with a 15 μm condenser aperture, yielding a probe diameter of 1.4 nm and semi-convergence angle of 2 mrad. The camera length was set to 320 mm to match the acceptance cone semi-angle at the bottom-mounted bright-field detector (Gatan model 805). Images of 1024 × 1024 pixels were recorded with a probe dwell time of 15.9 μs, yielding a frame exposure time of approximately 20 sec. Spatial sampling was set at 2.86 nm. Full Nyquist sampling would require steps <0.7 nm, so the undersampling was a compromise between resolution, field of view, and radiation exposure. Dose was measured at 1.4 electrons/$Å^2$ per dwell spot as described previously [19]. Total dose over the tilt series was thus 105 electrons /$Å^2$, which is comparable to a typical TEM acquisition. Single-axis tilt series were recorded using the FEI Xplore3D software from ±70º in 2º steps below 50º, and 1.5º

steps above 50º. Dynamic focus adjustment was employed to maintain focus conditions perpendicular to the tilt axis at all tilt angles.

2.3. Image processing

Tomographic reconstruction was performed by weighted back-projection in IMOD [23], using fiducial alignment with 15 nm gold beads added to grids before plunging. Further image processing was performed with ImageJ [24] and Bsoft [25]. For noise reduction only a weak 3D Gaussian blur filter was imposed (radius 1 or 1.4 pixel for Figures 1 and 2, respectively). IMOD and Chimera [26] were used for visualization. The bright-field image contrast was inverted for volume representation.

3. Results

Two STEM tilt series were selected to demonstrate the character and quality of the imaging. The reconstructions appear as Figures 1 and 2. The fibroblast cells are large (typical dimensions 60 × 12 μm) and well spread on the grid. The field of view (2.9 × 2.9 μm) thus includes only a small fraction of the total cell area, and the two chosen examples display somewhat different components. Following Hohmann-Marriott [22], we collected the STEM bright-field signal for its relative insensitivity to multiple scattering. After considerable experimentation, we present the data here as volume renderings of thick virtual sections. Note that the bright-field contrast has been inverted so that white represents dense mass while sparser regions appear transparent. This inversion allows us to see the denser features through the cellular volume.

The first reconstructed tomogram appears in Figure 1 in thick sequential sections containing 50 reconstructed planes each (140 nm total per section). At the substrate plane (Figure 1A), we observe mainly a mixture of small and large vesicles. Many of these vesicles show a punctate decoration, and other such puncta appear in the absence of membrane. Even without detailed analysis, some of the puncta appear brighter than others, and they clearly have internal structure that is not well resolved under the present conditions. In the central section (Figure 1B) we see primarily larger vesicles, including one vesicle completely enclosed in another and one multi-vesicular body. Two oriented fiber bundles lie along the axis of the cell extension. We identify these as acto-myosin stress fibers. Swaths of extracellular matrix parallel to the plasma membrane and perpendicular to the major cell axis appear at the upper surface outside the cell (Figure 1C). In the central section, individual actin microfilaments are observed running along the cell edge (Figure 1D). Within the multi-vesicular body, membrane-proximal structures are visible down to dimensions of 25 nm and less (Figure 1E). A stereo view (Figure 1F) integrates the visible features.

The tomogram in Figure 2 shows a number of additional features. Examining thinner virtual sections (15 planes, or 44 nm thickness per section) in this case, again parallel to the substrate, coated pits are visible at the basal surface. Two of these are expanded into orthogonal plane views in Figure 3A, B. A tight ring of protein projects into the cytoplasm. The membrane cap is faint due to its orientation; it is hidden by the tomographic missing wedge. However, the inner volume is easily distinguished by its very dark appearance. Clearly the contents of the pit, external to the cell, are more sparse or weakly scattering than the cytoplasm. This contrast serves to outline the pit from within. For comparison, we show an internal vesicle visible in the same plane. The heavy protein coat on the membrane is absent, and there is no difference in contrast between the vesicle lumen and

the cytoplasm.

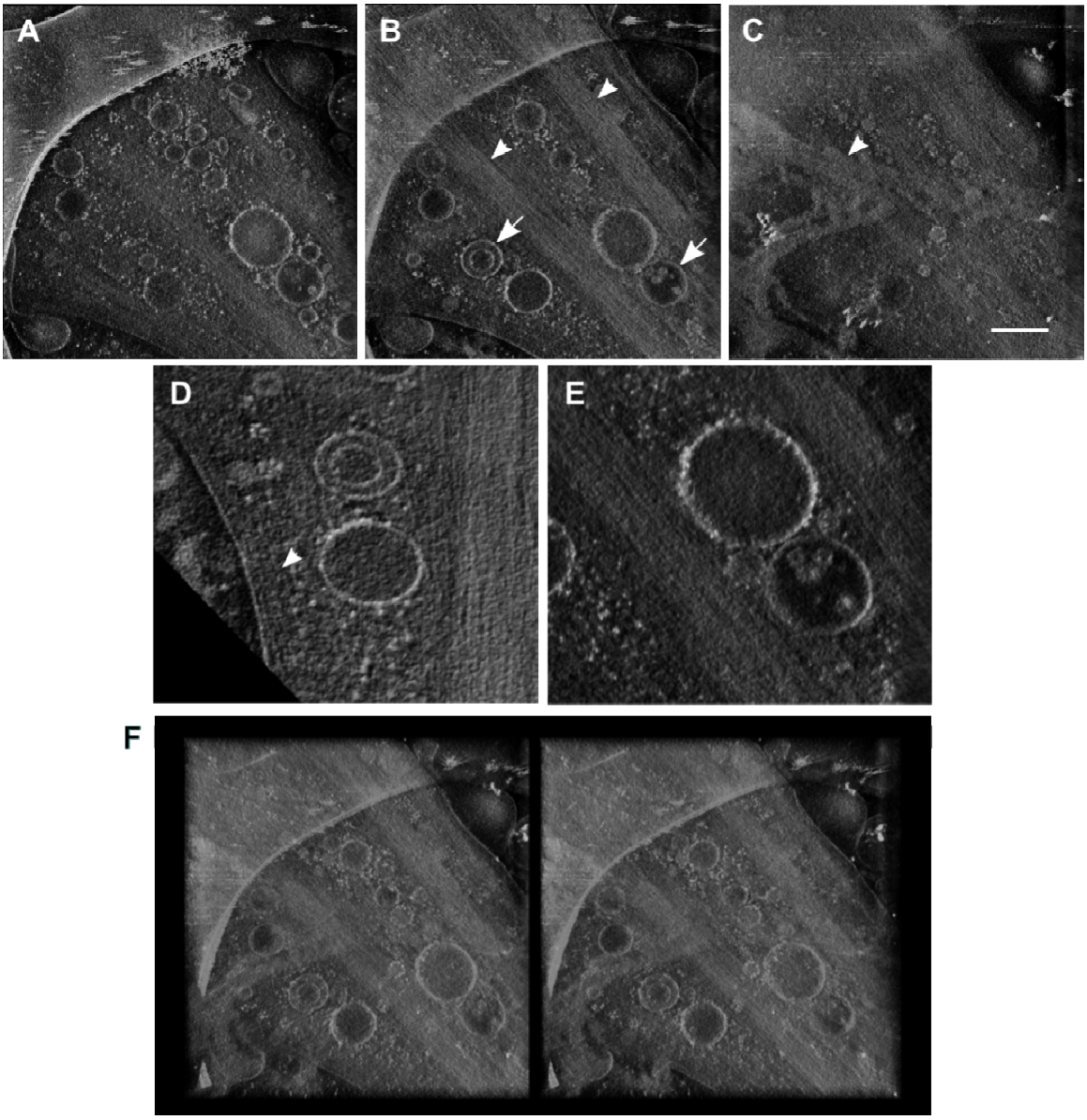

Figure 1. (A-C) Volume renderings of three non-overlapping, thick virtual sections (140 nm each, xy plane view) through a tomographic dataset (scale bar 500 nm). Cell thickness is 480 nm. (A) An abundance of small vesicles is seen adjacent to the growth substrate. (B) Nested and multilamellar vesicles (black arrows) and two thick acto-myosin stress fibers (white arrows) are found in this central section. (C) Extracellular matrix (white arrow) is seen at the free surface of the cell. (D, E) Details of the vesicle structures seen in B. Additionally, individual thin microfilaments are observed running parallel to the cell edge (white arrow). Similar filaments can be found fraying from the fiber bundle. (F) Wall-eye stereo view through the cell depth showing the spatial relation of visible features (field of view 2.9 × 2.9 μm).

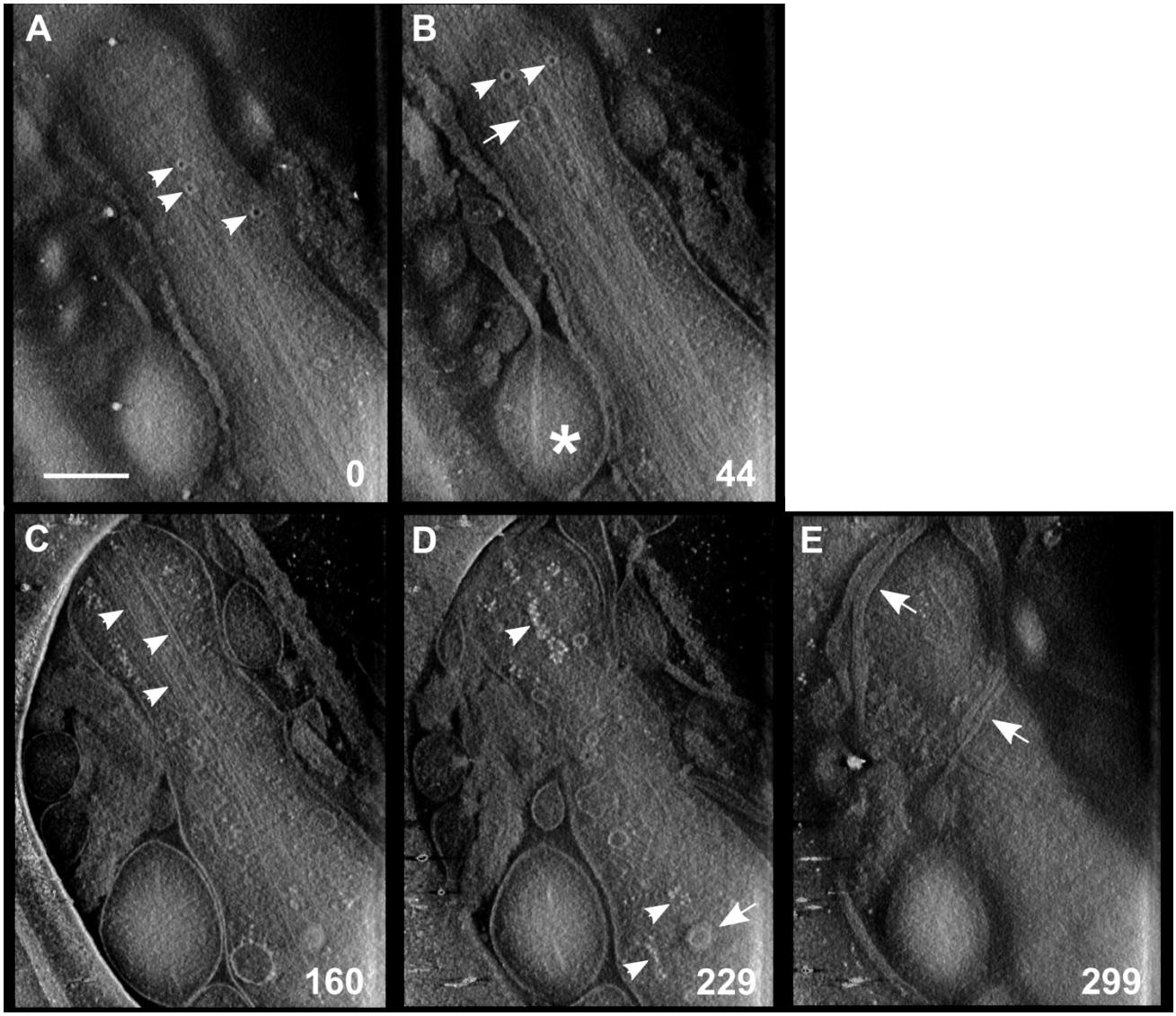

Figure 2. Volume renderings of non-overlapping sections (44 nm each, xy plane view). Cell thickness is 420 nm. Numbers in white represent the height in nm above the lowest plane (0) containing clearly visible structures. (A, B) Note the dense ring structures adjacent to the substrate (arrowheads). These appear to be incipient endocytotic vesicles, i.e., coated pits; their interior is completely dark. For comparison, an internal vesicle (arrow) has contrast similar to that of cytoplasm. Mycoplasma contamination appears in all sections (white asterisk). (C) A bundle of elongated membrane tubes (arrows) is found running along the cell axis. (D) Toward the plasma membrane we find small puncta of very high contrast, likely ribosomes (arrowheads). Most of these lie along rough endoplasmic reticulum. Among the vesicles observed in this plane, one bears a thick protein shell (arrow). (E) Tubular extensions of the mycoplasma are seen lying along the upper surface of the plasma membrane (arrows). These serve to delineate the upper surface of the cell, upon which considerable detail can be seen. Scale bar 500 nm.

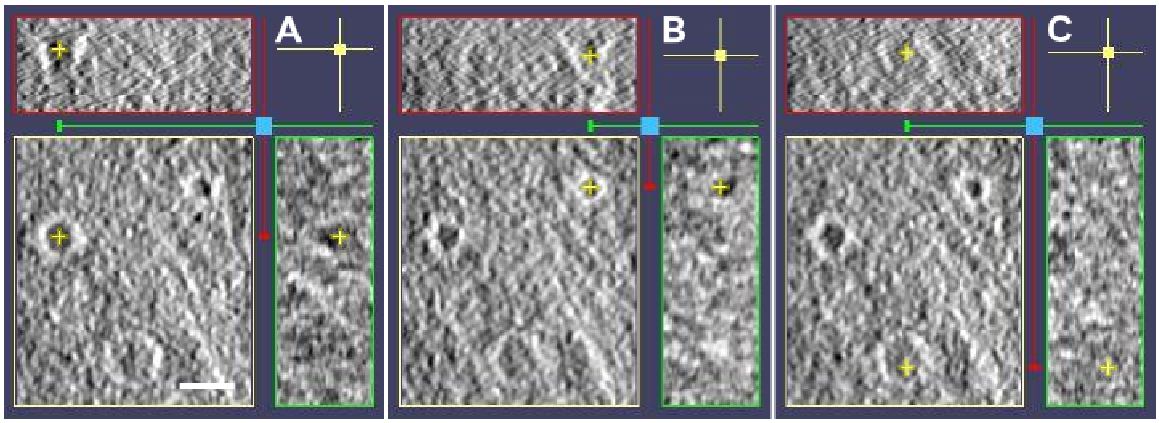

Figure 3. Endocytic vesicles in the process of pinching from the plasma membrane. A thick protein layer coats the neck of the pit. The figure shows the same horizontal field (xy) with different (xz, top) and (yz, right) cuts as marked by the yellow cross. (A, B) The interior of the pits (yellow crosses) remains contiguous with the exterior medium surrounding the cell, as seen by the dark (low scattering) contrast. (C) A cytoplasmic vesicle (yellow cross) lacks the heavy protein coat, and its interior has the same brightness as the surrounding cytoplasm. Scale bar 100 nm.

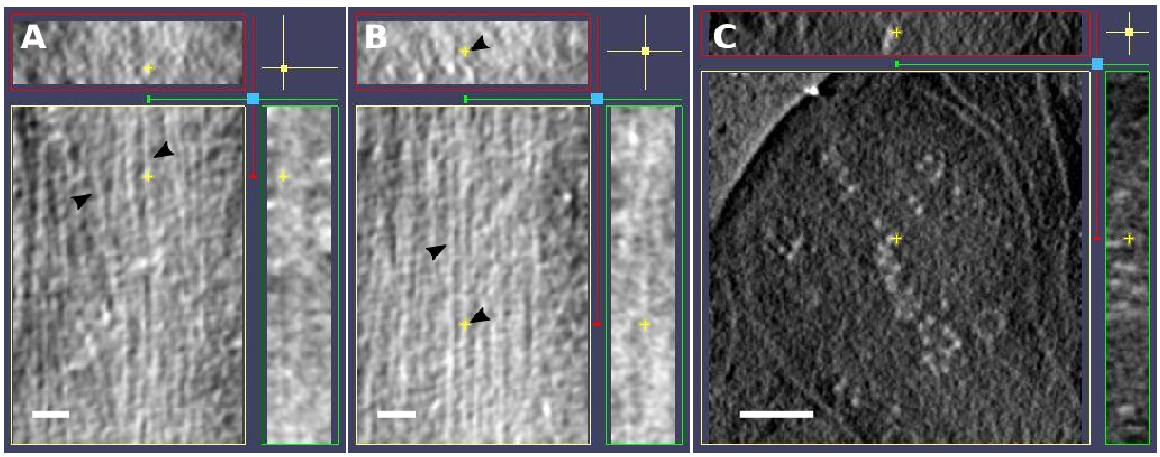

Figure 4. (A) Membrane tubules of endoplasmic reticulum (arrowheads) appear with variable width and angle. Scale bar 100 nm. (B) Interspersed among these tubules, we find more rigid tubes with diameter 25–28 nm, most likely microtubules (arrowheads). Scale bar 100 nm. (C) Ribosomes cluster around reticulated membrane. Other ribosomes appear to be free in the cytoplasm. Scale bar 200 nm.

Further toward the central plane in Figure 2 (160 nm plane), a bundle of membrane-delimited tubes is visible running along the cell axis. The expanded view in Figure 4A shows that the tubes have variable diameter with occasional forks and fusions. Interspersed with these membranes, straight tubes are seen with constant diameter of 25–28 nm, which can be identified tentatively as microtubules (Figure 4B). A cluster of bright puncta appears on a still higher plane (Figure 4C), similar to those in the first tomogram (Figure 2). Most of these puncta are associated with membranes. With dimensions of 20–30 nm and propensity for membrane association, these

structures appear to be ribosomes. We will return to the issue of their high contrast in the Discussion. Finally, outside the cell lie what appear to be contaminating mycoplasma. The cell bodies bulge from a network of tubular extensions. Two cells send such protrusions parallel to the upper surface of the fibroblast plasma membrane. At least one of these lipid tubes contains internal vesicles.

We can compare the observed features to conventionally embedded and stained thin sections, seen in Figure 5. The chosen section shows rough endoplasmic reticulum mixed with a variety of vesicles and possibly mitochondria. Here organelles are recognizable based on their characteristic morphologies and staining patterns. Although the image quality is good, empty white space arises from dehydration and resin embedding.

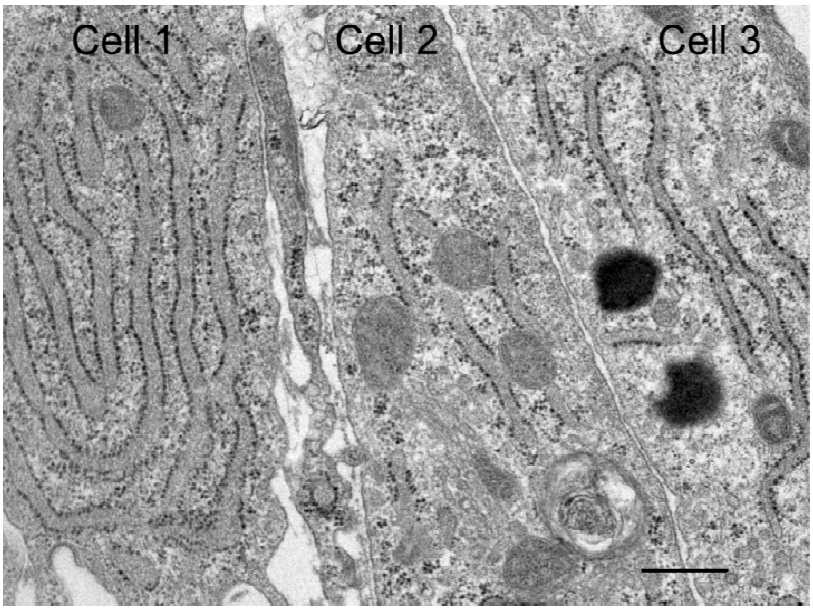

Figure 5. A conventionally-prepared thin section shows three adjacent cells filled with rough endoplasmic reticulum, numerous vesicles, and mitochondria. Scale bar 500 nm.

4. Discussion

From the data presented, it is clear that STEM offers a viable mode of tomographic imaging for eukaryotic cells. We have called the method CSTET, for cryo-scanning transmission electron tomography [19]. Specimens shown here were grown on gold Quantifoil grids and plunged into liquid ethane for vitrification, without chemical fixation, dehydration, or any other manipulation. The STEM reconstructions have a different qualitative texture than we have come to expect from defocus phase contrast TEM. This difference reflects the flat and monotonic optical transfer function, relative to the oscillatory CTF of defocus phase contrast. As a result, Fresnel fringes are minimized in STEM, while low spatial frequency information is retained. It is difficult to compare tomograms directly between STEM and TEM modes for samples such as those studied here because the cells are marginally too thick for reasonable quality zero-loss TEM tomography. In the available microscope operating at 200 kV with an energy-filtered CCD camera (Gatan Tridiem GIF), we were not able to obtain meaningful TEM tomograms.

Two features of STEM have major effects on image formation and should be emphasized. First, the imaging is done in focus. The depth of field is determined by the semi-convergence angle of the probe spot, which is in turn set by the condenser aperture size under the relevant (diffraction-limited) conditions. The settings described here provide a depth of field greater than one micron, so the entire thickness of the cell protrusion and edge remains in focus. Dynamic focusing is used to keep the entire field in focus at all tilt angles. Second, the STEM scattering signal is a quantitative measure of electron scattering. Through the illumination convergence angle and the acceptance angles of the detectors, which can be configured flexibly in STEM, deliberate choices can be made regarding collection of the scattered electrons. Such choices directly affect the mechanisms of contrast generation. In the present configuration, contrast represents primarily mass density, while there is also a component of elemental sensitivity. In the following discussion we elaborate on these issues.

4.1. Contrast Formation in TEM and STEM

Conventional TEM image contrast for biological materials is based on scattering from heavy metals, i.e., stain, within a plastic embedding medium. Scattering from the stain is blocked by an aperture placed in the objective back focal plane, as shown in Figure 6. The darkness of a spot in the image is thus proportional to the loss of intensity due to scattering.

Cryo-TEM is normally performed without metal staining, so contrast due to scattering is low. Image formation instead relies on phase contrast. The objective aperture is enlarged to permit passage of the weakly scattered electrons so that scattered and unscattered waves interfere at the image. Due to the 90° phase shift between them, the intensity contrast is minimal at focus. Defocus adds an additional relative path length and therefore phase to the scattered waves, generating contrast by interference. Density differences at nearby points create small differences in phase that then appear with different intensity in the image. For weak phase objects, the intensity variation as a function of phase can be approximately linear, in which case the image intensity is proportional to the material density traversed.

Defocus phase contrast entails the well-known complication that different spatial frequencies in the specimen are represented with different contrast: zero contrast for the lowest frequencies, then dark for matter and light for void, and then vice versa at higher frequencies, with tightening oscillations. Bright fringes resulting from the interference mechanism can accentuate the boundaries of membranes or filaments. Qualitatively, these fringes can be useful in outlining structures. They limit resolution, however, and they are not “real” in the sense that they do not reflect a negative mass density. The contrast transfer function is well defined and can be corrected straightforwardly for a thin sample. For a thick sample there will be a spread of defocus values, compounded by the change in defocus across the field when the sample is tilted. Correction of the CTF contrast transfer function for tomography is thus much more complex than for thin objects since different planes within the specimen require in principle different corrections [27–30]. Recently, phase plates have become available [5–8]. These provide contrast at low spatial frequencies by adding the 90° phase without defocus. However, the requirement for maintenance of phase coherence remains. As explained below, loss of phase coherence places a strict limit on specimen thickness.

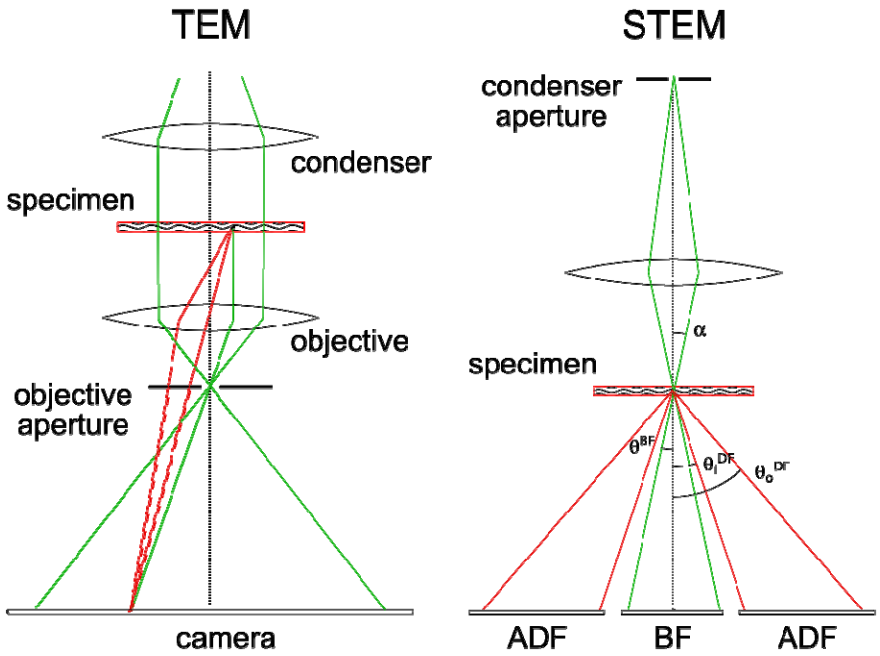

Figure 6. In conventionally stained and embedded TEM imaging, scattering from electron-dense metals is blocked by the objective aperture placed in the back focal plane. For locations in the specimen with strong scattering, i.e., a heavy stain concentration, blockage at the aperture produces a corresponding dark spot on the image. Cryo-TEM is normally performed without metal staining, so imaging relies on phase contrast as indicated by the dashed line. (See text for more detail.) In STEM the lenses are used to demagnify the condenser aperture into a probe spot focused on and scanned across the specimen. At each scan point the unscattered and scattered electrons are collected on bright-field and annular dark-field detectors, respectively. The illumination semi-convergence angle α determines the probe diameter and the depth of field. In the present configuration the outer cutoff of the bright-field detector (θ^{BF}) was set to match α, and the annular dark field detector (ADF) was not used. The light elements of biological materials scatter weakly and so dictate the use of small angles.

In STEM, the microscope lenses are used to demagnify the condenser aperture into a probe spot focused on and scanned across the specimen. STEM is similar in this sense to a laser scanning confocal microscope, or indeed to a conventional scanning electron microscope. Many modern TEM instruments are also STEM-capable. The illumination semi-convergence angle α determines probe diameter and the depth of field (similarly to the numerical aperture in the light microscope, up to limitations imposed by spherical aberration). At each scan point the unscattered and scattered electrons are collected on disk-shaped bright-field and annular dark-field detectors, respectively (see Figure 6). In the present configuration the outer cutoff of the bright-field detector (θ^{BF}) was set to match α, and the annular dark field detector (ADF) was not used. To the extent that electrons are scattered away from the bright-field collection angles, the corresponding pixel appears dark in the image.

Every chemical element produces a characteristic scattering pattern depending primarily on the number of protons, i.e., the atomic number Z [31]. Heavier elements scatter more strongly and to higher angles. Weak scattering by the light elements of biological materials dictates the use of small collection angles for bright field imaging. The quantitative nature of the STEM signal is best exemplified in mass measurements of biomolecules and molecular complexes [32,33]. While generally these employed freeze-dried material, one pioneering work was performed cryogenically with vitrified specimens [34].

Additional criteria acquire importance when considering thick specimens for tomography. First and foremost is the requirement for phase coherence to produce phase contrast in TEM. Inelastic scattering processes entail by definition a loss of energy and a change in the wavelength of the outgoing electrons. Due to chromatic aberration in the microscope optics, these electrons do not come to focus at the same plane as those that experienced only elastic scattering. Effectively this causes a loss of phase coherence at the camera plane and an out-of-focus haze in the image. The haze can be effectively removed using a spectrometer that restricts image formation strictly to elastically scattered electrons, the so-called "zero-loss" imaging in energy-filtered TEM. This procedure introduces another sort of absorption contrast, with the spectrometer replacing the objective aperture and a loss of signal in proportion to the fraction of inelastic scattering rather than the elastic as for conventional TEM [35].

While zero-loss filtering removes image haze and accentuates the component of phase contrast, the specimen still suffers radiation damage from the inelastic processes. The characteristic absorption length sets a natural scale for the specimen thickness suitable for phase contrast tomography: the mean free path for inelastic scattering. This is roughly 250 nm for biological material embedded in vitrified water, for electrons with 200 kV accelerating voltage [36]. Then half the signal is used to form the image, while half is lost to the spectrometer. The loss worsens when the sample is tilted to obtain 3D information. Geometric doubling of the effective thickness at 60° tilt (for a flat slab) leaves only a quarter of the intensity to the image. For a sample of 500 nm thickness, only 1/16 of the signal remains. High tilt images therefore suffer much worse signal-to-noise ratio than the lower tilts, so the information required for reconstruction in the third dimension is of lower quality for thicker specimens. In principle, the correction of chromatic aberration should permit a restoration of the lost phase signal [37]. However, such microscopes are exceedingly rare and expensive.

STEM imaging offers an attractive alternative for tomography of thicker specimens, especially due to the long depth of field alluded to above. Depth of field follows directly from the choice of condenser aperture: the smaller the aperture, the shallower the convergence angle, the longer the depth of field, and the broader the probe spot. Of course long depth of field comes at the expense of lateral resolution; a broader probe provides lower resolution. For tomography, a compromise should be found between resolution and accessible specimen thickness. Importantly, since the sample is illuminated point by point, phase coherence is not required for image formation.

Recently the application of STEM tomography was extended to cryogenic specimens [19]. In general there had been a strong case against STEM for cryo-imaging: for a given electron dose the interferometric nature of the TEM modality offers stronger contrast from the weakly scattering light elements that comprise biological material [31,38]. However, other considerations become important for thicknesses comparable to or exceeding the mean free path for inelastic scattering. These are precisely the scales relevant to cellular tomography. In fact, the advantages of STEM are, perhaps ironically, most important for unfixed, vitrified cellular specimens lacking heavy metal stain. The

important physical insight is that inelastic scattering is predominantly forward-directed. As a result, the scattered intensity recorded by the STEM detectors reflects mainly the elastic interactions, and inelastic interactions do not deflect the signal from one detector to the other. Unlike in phase contrast there is no need to filter the electrons energetically. Therefore, all the incident flux to which the specimen is exposed can contribute to form the image. Since the atomic numbers of the three major elements in cell specimens are similar (Z = 6, 7, 8 for C, N, O), the signal at a point in the image is a measure of the number of scattering atoms in a one-dimensional projection through the specimen. Tomographic reconstruction then provides a map of the mass density in 3D.

4.2. Prospects for Cryo-STEM Tomography

A full quantitative analysis of cryo-STEM tomography contrast will have to involve an account for the missing wedge effect, which is reduced in STEM but not absent, as well as top-bottom effects due to spreading of the probe beam within the sample. Generally we find that membrane and protein structures such as actin filaments and extracellular matrix appear roughly equally bright (or dark) on the background of cytoplasm. Ribosomes, however, appear much brighter (more strongly scattering) than any other cellular component in the field of view (e.g., Figure 4C). We attribute this to the phosphorus content of the RNA. Phosphorus has atomic number Z = 15. One can expect the total scattering to vary roughly as $Z^{3/2}$ [32], so scattering from P will be approximately 4 times stronger than from C. "Z contrast" was demonstrated long ago for imaging of unstained, resin-embedded sections [39]. The method is well known in materials science [40] and can be used to differentiate even single atoms at high resolution [41]. We have taken this approach recently to examine the bacterial poly-phosphate body [42]. In future work it will be interesting to return to the ribosomes to take advantage of this contrast at maximal resolution and with sub-tomogram averaging techniques.

One current challenge in STEM practice is to record both bright- and dark-field signals simultaneously. In our microscope, there are two separate detectors (from different manufacturers) that collect the two signals, but the relative cutoff angles are set by hardware geometry, and a gap invariably remains in the angular collection range. This present frustration indicates an obvious point for improvement. Collecting both signals simultaneously would at the very least improve noise statistics, or reduce exposure. Moreover, there is great potential to exploit the Z contrast with differential angular measurements or a radially segmented detector for elemental mapping within the cell.

In practice, one of the most significant challenges for imaging of thick cells is simply to choose the area of interest. Little contrast is obtained in projection because of the many overlapping features. Therefore selection of regions for tilt series collection may benefit from a correlative approach, as practiced already in other methods. Possibly the closest model will be that developed for the soft X-ray microscope, where cells expressing fluorescent protein are first mapped in a cryo-light microscope [43,44]. In the present study the selection of regions for image collection was based on rather subjective impressions of the projection images. Only after reconstruction did the richness of internal details emerge.

5. Conclusion

This work effectively demonstrates CSTET as a viable and informative technique for

cryo-tomography of intact eukaryotic cells. Cells were vitrified *in situ* without fixation or permeabilization. Membranes, organelles, and cytoskeleton are clearly visible throughout the examined cell protrusions. The texture of the reconstructions differs qualitatively from the more familiar defocus phase imaging tomography because they do not pass the spatial filtering effects of the CTF. On one hand the low frequencies remain, and on the other hand Fresnel fringes and contrast inversions are absent. These features allow for effective representation of the mass density in a brightness/transparency mode especially suited to volume imaging. They also enable interpretation of STEM voxel values in terms of local properties, as is possible also in soft X-ray cryo-tomography [45]. TEM, STEM, and soft X-ray tomographic methods exhibit specific advantages in complementary realms of application. The least explored option to date, CSTET holds great potential to extend the specimen thickness range as well as to introduce quantitative and analytical image interpretation in electron tomography.

Acknowledgments

The authors are grateful to Lothar Houben, Peter Rez, and Nadav Elad for enlightening discussions. This work was funded in part by a grant from the Israel Science Foundation, by the Gerhardt M.J. Schmidt Minerva Center for Supramolecular Architecture, and by the Irving and Cherna Moskowitz Center for Nano and Bio-Nano Imaging. The lab of ME has benefited from the historical generosity of the Harold Perlman family.

Conflict of Interest

All authors declare no conflicts of interest in this paper.

References

1. Bai X, McMullan G, Scheres SHW (2015) How cryo-EM is revolutionizing structural biology. *Trends Biochem Sci* 40: 49–57.
2. Kühlbrandt W. (2014) Cryo-EM enters a new era. *eLife* 3: e03678.
3. Briegel A, Dias DP, Li Z, et al. (2006) Multiple large filament bundles observed in Caulobactercrescentus by electron cryotomography. *Mol Microbiol* 62: 5–14.
4. Henderson GP, Gan L, Jensen GJ (2007) 3-D ultrastructure of O. tauri: electron cryotomography of an entire eukaryotic cell. *PloS One* 2: e749.
5. Danev R, Kanamaru S, Marko M, et al. (2010) Zernike phase contrast cryo-electron tomography. *J Struct Biol* 171: 174–181.
6. Murata K, Liu X, Danev R, et al. (2010) Zernike Phase Contrast Cryo-Electron Microscopy and Tomography for Structure Determination at Nanometer and Subnanometer Resolutions. *Structure* 18: 903–912.
7. Guerrero-Ferreira RC, Wright ER (2014) Zernike phase contrast cryo-electron tomography of whole bacterial cells. *J Struct Biol* 185: 129–133.
8. Danev R, Buijsse B, Khoshouei M, et al. (2014) Volta potential phase plate for in-focus phase contrast transmission electron microscopy. *P Natl Acad Sci U S A* 111: 15635–15640.

9. Briggs JAG (2013) Structural biology in situ--the potential of subtomogram averaging. *Curr Opin Struct Biol* 23: 261–267.
10. Marko M, Hsieh C, Schalek R, et al. (2007) Focused-ion-beam thinning of frozen-hydrated biological specimens for cryo-electron microscopy. *Nat Methods* 4: 215–217.
11. Hsieh C, Schmelzer T, Kishchenko G, et al. (2014) Practical workflow for cryo focused-ion-beam milling of tissues and cells for cryo-TEM tomography. *J Struct Biol* 185: 32–41.
12. Rigort A, Bäuerlein FJB, Villa E, et al. (2012) Focused ion beam micromachining of eukaryotic cells for cryoelectron tomography. *P Natl Acad Sci U S A* 109: 4449–4454.
13. Kapishnikov S, Weiner A, Shimoni E, et al. (2012) Oriented nucleation of hemozoin at the digestive vacuole membrane in Plasmodium falciparum. *P Natl Acad Sci U S A* 109: 11188–11193.
14. Müller WG, Heymann JB, Nagashima K, et al. (2012) Towards an atlas of mammalian cell ultrastructure by cryo soft X-ray tomography. *J Struct Biol* 177: 179–192.
15. Carzaniga R, Domart M-C, Collinson LM, et al. (2014) Cryo-soft X-ray tomography: a journey into the world of the native-state cell. *Protoplasma* 251: 449–458.
16. Cruz-Adalia A, Ramirez-Santiago G, Calabia-Linares C, et al. (2014) T cells kill bacteria captured by transinfection from dendritic cells and confer protection in mice. *Cell Host Microbe* 15: 611–622.
17. Do M, Isaacson SA, McDermott G, et al. (2015) Imaging and characterizing cells using tomography. Arch Biochem Biophys. in press, eprint doi:10.1016/j.abb.2015.01.011
18. Schertel A, Snaidero N, Han H-M, et al. (2013) Cryo FIB-SEM: Volume imaging of cellular ultrastructure in native frozen specimens. *J Struct Biol* 184: 355–360.
19. Wolf SG, Houben L, Elbaum M (2014) Cryo-scanning transmission electron tomography of vitrified cells. *Nat Methods* 11: 423–428.
20. Yakushevska AE, Lebbink MN, Geerts WJC, et al. (2007) STEM tomography in cell biology. *J Struct Biol* 159: 381–391.
21. Aoyama K, Takagi T, Hirase A, Miyazawa A (2008) STEM tomography for thick biological specimens. *Ultramicroscopy* 109: 70–80.
22. Hohmann-Marriott MF, Sousa AA, Azari AA, et al. (2009) Nanoscale 3D cellular imaging by axial scanning transmission electron tomography. *Nat Methods* 6: 729–731.
23. Kremer JR, Mastronarde DN, McIntosh JR (1996) Computer visualization of three-dimensional image data using IMOD. *J Struct Biol* 116: 71–76.
24. Schneider CA, Rasband WS, Eliceiri KW (2012) NIH Image to ImageJ: 25 years of image analysis. *Nat Methods* 9: 671–675.
25. Heymann JB, Belnap DM (2007) Bsoft: image processing and molecular modeling for electron microscopy. *J Struct Biol* 157: 3–18.
26. Pettersen EF, Goddard TD, Huang CC, et al. (2004) UCSF Chimera--a visualization system for exploratory research and analysis. *J Comput Chem* 25: 1605–1612.
27. Jensen GJ, Kornberg RD (2000) Defocus-gradient corrected back-projection. *Ultramicroscopy* 84: 57–64.
28. Philippsen A, Engel H-A, Engel A (2007) The contrast-imaging function for tilted specimens. *Ultramicroscopy* 107: 202–212.
29. Zanetti G, Riches JD, Fuller SD, et al. (2009) Contrast transfer function correction applied to cryo-electron tomography and sub-tomogram averaging. *J Struct Biol* 168: 305–312.

30. Voortman LM, Franken EM, van Vliet LJ, et al. (2012) Fast, spatially varying CTF correction in TEM. *Ultramicroscopy* 118: 26–34.
31. Rez P (2003) Comparison of phase contrast transmission electron microscopy with optimized scanning transmission annular dark field imaging for protein imaging. *Ultramicroscopy* 96: 117–124.
32. Engel A (2009) Chapter 9 Scanning Transmission Electron Microscopy: Biological Applications. *Adv Imag Elect Phys* 159: 357–386.
33. Reichelt R, Holzenburg A, Buhle EL, et al. (1990) Correlation between structure and mass distribution of the nuclear pore complex and of distinct pore complex components. *J Cell Biol* 110: 883–894.
34. Trachtenberg S, Leonard KR, Tichelaar W (1992) Radial mass density functions of vitrified helical specimens determined by scanning transmission electron microscopy: their potential use as substitutes for equatorial data. *Ultramicroscopy* 45: 307–321.
35. Angert I, Majorovits E, Schröder RR (2000) Zero-loss image formation and modified contrast transfer theory in EFTEM. *Ultramicroscopy* 81: 203–222.
36. Grimm R, Typke D, Bärmann M, et al. (1996) Determination of the inelastic mean free path in ice by examination of tilted vesicles and automated most probable loss imaging. *Ultramicroscopy* 63: 169–179.
37. Baudoin JP, Jinschek JR, Boothroyd CB, et al. (2013) Chromatic aberration-corrected tilt series transmission electron microscopy of nanoparticles in a whole mount macrophage cell. *Microsc Microanal* 19: 814–820.
38. Henderson R (1995) The potential and limitations of neutrons, electrons and X-rays for atomic resolution microscopy of unstained biological molecules. *Q Rev Biophys* 28: 171–193.
39. Pennycook SJ (1989) Z-contrast stem for materials science. *Ultramicroscopy* 30: 58–69.
40. Carlemalm E, Kellenberger E (1982) The reproducible observation of unstained embedded cellular material in thin sections: visualisation of an integral membrane protein by a new mode of imaging for STEM. *EMBO J* 1: 63–67.
41. Krivanek OL, Chisholm MF, Nicolosi V, et al. (2010) Atom-by-atom structural and chemical analysis by annular dark-field electron microscopy. *Nature* 464: 571–574.
42. Wolf SG, Rez P, Elbaum M (2015) Phosphorus detection in vitrified bacteria by cryo-STEM annular dark field analysis. *J Microscopy* doi/10.1111/jmi.12289 (e-print, in press).
43. Hagen C, Guttmann P, Klupp B, et al. (2012) Correlative VIS-fluorescence and soft X-ray cryo-microscopy/tomography of adherent cells. *J Struct Biol* 177: 193–201.
44. Duke EMH, Razi M, Weston A, et al. (2014) Imaging endosomes and autophagosomes in whole mammalian cells using correlative cryo-fluorescence and cryo-soft X-ray microscopy (cryo-CLXM). *Ultramicroscopy* 143: 77–87.
45. Kapishnikov S, Weiner A, Shimoni E, et al. (2013) Digestive Vacuole Membrane in Plasmodium falciparum-Infected Erythrocytes: Relevance to Templated Nucleation of Hemozoin. *Langmuir* 29: 14595–14602.

AIMS Press